SHELL CLOSURES, LOOSELY BOUND STRUCTURES, AND HALOS IN EXOTIC NUCLEI

G. Saxena [a,b*], *D. Singh* [b]

[a] *Department of Physics, Govt. Women Engineering College*
Ajmer-305002, India

[b] *Department of Physics, University of Rajasthan*
Jaipur-302004, India

Inspired by the recent experiments [1, 2] indicating doubly magic nuclei that lie near the drip-line and encouraged by the success of our relativistic mean-field (RMF) plus state-dependent BCS approach to the description of the ground-state properties of drip-line nuclei, we develop this approach further, across the entire periodic table, to explore magic nuclei, loosely bound structures, and halo formation in exotic nuclei. In our RMF+BCS approach, the single-particle continuum corresponding to the RMF is replaced by a set of discrete positive-energy states for the calculations of pairing energy. Detailed analysis of the single-particle spectrum, pairing energies, and densities of the nuclei predict the unusual proton shell closures at proton numbers $Z = 6$, 14, 16, 34, and unusual neutron shell closures at neutron numbers $N = 6$, 14, 16, 34, 40, 70, 112. Further, in several nuclei, like the neutron-rich isotopes of Ca, Zr, Mo, etc., the gradual filling of low-lying single-particle resonant state together with weakly bound single-particle states lying close to the continuum threshold helps accommodate more neutrons but with an extremely small increase in the binding energy. This gives rise to the occurrence of loosely bound systems of neutron-rich nuclei with a large neutron-to-proton ratio. In general, the halo-like formation, irrespective of the existence of any resonant state, is seen to be due to the large spatial extension of the wave functions for the weakly bound single-particle states with low orbital angular momentum having very small or no centrifugal barriers.

1. INTRODUCTION

Experimental and theoretical studies of exotic nuclei with extreme isospin values constitute one of the most active current areas of research in nuclear physics. Experiments [1–7] with radioactive nuclear beams allow studying very short-lived nuclei with large $|N - Z|$ values. Especially, the neutron-rich nuclei with unusually large isospin values are known to exhibit several interesting features. For nuclei close to the neutron drip-line, the neutron density distribution shows a much extended tail with a diffused neutron skin while the Fermi level lies close to the single-particle continuum [6]. In some cases, this may even lead to the phenomenon of a neutron halo, as observed in the case of light nuclei [5, 6, 8], made of several neutrons outside a core with the separation energy of the order of 100 keV or

less. Interestingly, the possibility of the occurrence of such structures was discussed by Migdal [9] already in the early 1970s. Obviously, for such nuclei, due to the weak binding and large spatial dimension of the outermost nucleons, the role of continuum states and their coupling to the bound states become exceedingly important, especially for the pairing energy contribution to the total binding energy of the system. Further, in recent experiments with radioactive nuclear beams, disappearance of traditional magic numbers and appearance of new magic numbers have been observed in nuclei with exotic isospin ratios [6, 7]. Recently, it has been demonstrated in two independent experiments [3, 4] that ^{24}O, the heaviest isotope of oxygen with the neutron number $N = 16$, is a doubly magic nucleus. More recently, ^{100}Sn was also found to be a doubly magic nucleus [1] and the reaction cross section of ^{22}C, the drip-line nucleus, turned out to be significantly larger than those of its neighboring isotopes, suggesting that ^{22}C is a halo nucleus [5].

*E-mail: gauravphy@gmail.com

Theoretical descriptions of drip-line nuclei in terms of a few-body model or clusters [8, 10], shell model [11, 12], and mean-field theories, both nonrelativistic [13, 14] and relativistic mean field (RMF) [15–30] have been well obtained. The advantage of the RMF approach is that it provides the spin–orbit interaction in the entire mass region, which is consistent with the nuclear density [19]. This indeed has been found to be very important for the study of unstable nuclei near the drip-line [18]. It was recently shown in [26, 27] that the RMF plus BCS approach wherein the continuum is replaced by the discrete single-particle states for the calculation of the pairing energy provides an alternative fast approach to the relativistic Hartree–Fock–Bogoliubov (HFB) description [21, 25] of the drip-line nuclei. In particular, it was demonstrated in [26, 27] that the resonant states that lie close to zero energy in the continuum and gradually come down to become bound with an increasing neutron number play the crucial role in producing extremely neutron-rich loosely bound nuclei due to coupling of these resonant states with the bound states near the Fermi level through the pairing interaction. Evidently, the concentration of the major part of the wave function of the resonant state within the potential well and its proximity to the Fermi surface, while being close to zero energy, provide a favorable condition for the existence of extremely neutron-rich nuclei. This was amply demonstrated in [26, 27] for the neutron-rich isotopes of Ca, Ni, Zr, Sn and Pb nuclei.

Moreover, it has been shown [26] that irrespective of whether any resonant state exists, the occupancy of weakly bound neutron single-particle states having low orbital angular momentum ($l = 0$ or $l = 1$), with a well-spread wave function due to the absence or a very small strength of centrifugal barrier, is conducive to the occurrence of nuclei with a widely extended neutron density. Such nuclei are found to have characteristically very small two-neutron separation energy and a large neutron rms radius akin to that observed in halo systems. The role of pairing correlations described here is found to be consistent with the conclusions of nonrelativistic HFB studies of neutron-rich weakly bound nuclei discussed recently in [13].

Encouraged by the success of our RMF+BCS approach [26] and the impetus provided by the recent experimental developments, especially the measurements in [1–5], we use it to study the structure of even–even nuclei covering the whole periodic region up to the drip-lines to investigate the unusual proton and neutron magic numbers and doubly magic nucleus and also to identify the weakly bound nuclei with large skin or

halo formation. For simplicity and transparency, we do not consider the deformation degree of freedom. Indeed, by using such an approach, we intend to use the advantage offered by the analysis of results in terms of spherical single-particle wave functions. This is especially true for the understanding of shell closures and magicity, and behavior of single-particle states near the Fermi surface, which in turn plays an important role in producing weakly bound systems and halo structures. Similarly, within such a framework, the contributions of neutron and proton single-particle states to the density profiles, pairing gaps, total pairing energy etc. which are also equally important in the study of shell closures and halo structures, can be demonstrated with clarity. These aspects of the spherical framework indeed make this approach very useful especially for the study of poorly understood exotic nuclei. Nevertheless, we eventually compare our results with those of the RMF calculations taking deformation into account [30], in particular, for the magic nuclei, to check if these nuclei persist to be spherical due to the proton and neutron shell closures.

This paper is organized as follows. In Sec. 2, a brief description of the RMF model [18, 26] is given. Section 3 is devoted to the discussion of our results obtained with the thermomechanical analysis (TMA) force parameterization. As a representative example of extensive calculations, we describe and analyze the results of our calculations for the chain of Si isotopes. This is followed by a brief description of the main results of similar analyses for other nuclei exhibiting unusual shell closures and magicity as well as those representing loosely bound system with appreciable neutron skin or even a halo formation. Finally, Sec. 4 provides a summary of our results and conclusions.

2. RELATIVISTIC MEAN-FIELD MODEL

Our RMF calculations are carried out using the model Lagrangian density with nonlinear terms both for the σ and ω mesons along with the TMA parameterization described in detail in Refs. [18, 26],

$$\mathcal{L} = \bar{\psi}[i\gamma^\mu \partial_\mu - M]\psi +$$
$$+ \frac{1}{2}\partial_\mu \sigma \partial^\mu \sigma - \frac{1}{2}m_\sigma^2 \sigma^2 - \frac{1}{3}g_2 \sigma^3 - \frac{1}{4}g_3 \sigma^4 - g_\sigma \bar{\psi}\sigma\psi -$$
$$- \frac{1}{4}H_{\mu\nu}H^{\mu\nu} + \frac{1}{2}m_\omega^2 \omega_\mu \omega^\mu + \frac{1}{4}c_3(\omega_\mu \omega^\mu)^2 - g_\omega \bar{\psi}\gamma^\mu \psi \omega_\mu -$$
$$- \frac{1}{4}G_{\mu\nu}^a G^{a\mu\nu} + \frac{1}{2}m_\rho^2 \rho_\mu^a \rho^{a\mu} - g_\rho \bar{\psi}\gamma_\mu \tau^a \psi \rho^{\mu a} -$$
$$- \frac{1}{4}F_{\mu\nu}F^{\mu\nu} - e\bar{\psi}\gamma_\mu \frac{1-\tau_3}{2}A^\mu \psi, \quad (1)$$

where the field tensors H, G, and F for the vector fields are defined by

$$H_{\mu\nu} = \partial_\mu \omega_\nu - \partial_\nu \omega_\mu,$$
$$G^a_{\mu\nu} = \partial_\mu \rho^a_\nu - \partial_\nu \rho^a_\mu - 2g_\rho\, \epsilon^{abc} \rho^b_\mu \rho^c_\nu,$$
$$F_{\mu\nu} = \partial_\mu A_\nu - \partial_\nu A_\mu,$$

and other symbols have their usual meaning. As usual, these RMF calculations are performed assuming "nosea" treatment [17], which amounts to neglecting the effects of the Dirac sea.

Based on the single-particle spectrum calculated by the RMF described above, we perform a state-dependent BCS calculations [31, 32]. As we already mentioned, the continuum is replaced by a set of positive-energy states generated by placing the nucleus in a spherical box. Then the gap equations have the standard form for all the single-particle states, i. e.,

$$\Delta_{j_1} = -\frac{1}{2}\, \frac{1}{\sqrt{2j_1 + 1}} \sum_{j_2} \frac{\left\langle (j_1{}^2)\, 0^+ \,|V|\, (j_2{}^2)\, 0^+ \right\rangle}{\sqrt{\left(\varepsilon_{j_2} - \lambda\right)^2 + \Delta_{j_2}^2}} \times$$
$$\times \sqrt{2j_2 + 1}\, \Delta_{j_2}, \quad (2)$$

where ε_{j_2} are the single-particle energies and λ is the Fermi energy, whereas the particle number condition is given by $\sum_j (2j + 1)v_j^2 = N$. In the calculations, we use a delta force for the pairing interaction, i. e., $V = -V_0 \delta(r)$ with the same strength V_0 for both protons and neutrons. The value of the interaction strength $V_0 = 350$ MeV fm³ was determined in Refs. [26, 27] by obtaining a best fit to the binding energy of Ni isotopes. We use the same value of V_0 for our present studies of isotopes of other nuclei. Apart from its simplicity, the applicability and justification of using such a δ-function form of interaction was recently discussed in Refs. [13], where it has been shown in the context of HFB calculations that the use of a delta force in a finite space simulates the effect of finite-range interaction in a phenomenological manner (see also Refs. [33, 34] for more details). The pairing matrix element for the δ-function force is given by

$$\left\langle (j_1{}^2)\, 0^+ \,|V|\, (j_2{}^2)\, 0^+ \right\rangle =$$
$$= -\frac{V_0}{8\pi} \sqrt{(2j_1 + 1)(2j_2 + 1)}\, I_R, \quad (3)$$

where

$$I_R = \int dr \frac{1}{r^2} \left(G^\star_{j_1} G_{j_2} + F^\star_{j_1} F_{j_2} \right)^2 \quad (4)$$

is the radial integral. Here, G_α and F_α denote the respective radial wave functions for the upper and lower components of the nucleon wave function expressed as

$$\psi_\alpha = \frac{1}{r} \begin{pmatrix} i\, G_\alpha\ \mathcal{Y}_{j_\alpha l_\alpha m_\alpha} \\ F_\alpha\ \sigma \cdot \hat{r}\ \mathcal{Y}_{j_\alpha l_\alpha m_\alpha} \end{pmatrix}, \quad (5)$$

and satisfy the normalization condition

$$\int dr \{ |G_\alpha|^2 + |F_\alpha|^2 \} = 1. \quad (6)$$

In Eq. (5), the symbol $\mathcal{Y}_{jlm}$ is used for the standard spinor spherical harmonics with the phase i^l. The coupled field equations obtained from the Lagrangian density in (1) are finally reduced to a set of simple radial equations [17], which are solved self-consistently along with the equations for the state-dependent pairing gap Δ_j and the total particle number N for a given nucleus.

3. RESULTS AND DISCUSSION

In what follows, as a representative example, we first discuss our RMF results for the entire chain of $^{22-48}$Si isotopes; the predicted lightest and heaviest bound isotopes amongst these are respectively ^{22}Si and ^{48}Si. Interestingly, the results for the proton pairing gaps, their pairing energy, proton single-particle spectra, and the proton density profiles show that the proton shell closure occurs for all the isotopes of Si consistently at $Z = 14$. The fully occupied proton single-particle states are $1s_{1/2}$, $1p_{3/2}$, $1p_{1/2}$, and $1d_{5/2}$. However, the lightest isotope ^{22}Si is found to be just bound. Indeed, for this proton-rich isotope, due to a large Coulomb interaction, the proton single-particle potential becomes quite shallow and the proton Fermi level, having the energy $\epsilon_F = 0.58$ MeV, lies just above the continuum threshold, whereas the last bound proton single-particle state $1d_{5/2}$ is bound just by 0.71 MeV. The pairing energy contribution from protons for all the isotopes indeed remains zero throughout. This unusual magicity at $Z = 14$ is found to be due to a large gap between the proton single-particle state $1d_{5/2}$ and the other two single-particle states $1d_{3/2}$ and the $2s_{1/2}$ in the s–d shell. This conclusion is also supported by the rapidly decreasing proton density for all the isotopes within a short radial distance.

In order to also demonstrate the probable neutron shell closures in these isotopes, and hence identify the doubly magic nuclei, we show in Fig. 1 the variation in the pairing energy E_p from neutrons (the proton contribution being zero for all the Si isotopes), the two-neutron separation energy S_{2n}, and the neutron single-particle energy E_{sp} for the entire chain of Si isotopes
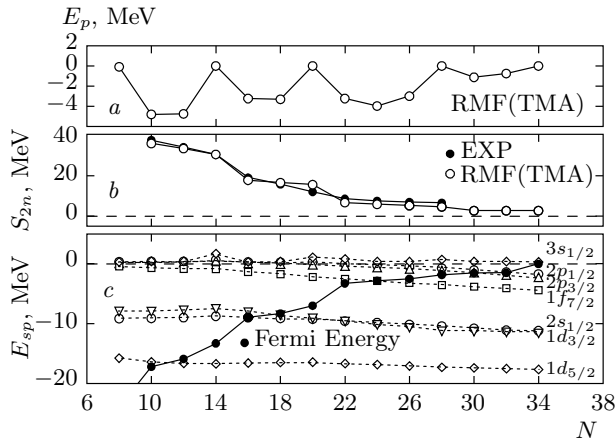
Fig. 1. RMF+BCS results for the Si isotopes showing the neutron number N dependence of the (a) total pairing energy, (b) two-neutron separation energy and its comparison with the available experimental data [35], and (c) relevant neutron single-particle energy spectrum along with the position of the neutron Fermi energy depicted by solid circles and connected by solid line

as a function of the neutron number N. As can be seen in Fig. 1a, the neutron pairing energy also vanishes for each of the Si isotopes with neutron numbers $N = 8$, 14, 20, 28, 34, indicating the shell closures for both the protons and neutrons. Thus, for the proton magic number at $Z = 14$, apart from the traditional neutron shell closures at $N = 8$, 20, 28, new shell closures appear at $N = 14$, 34, making the ^{22,28,34,42,48}Si isotopes doubly magic.

These single-particle shell structures revealed by the neutron dependence of the pairing energy are also exhibited in the variation of two-neutron separation energies, S_{2n}, shown in Fig. 1b. An abrupt decrease in the S_{2n} value for the isotopes with a neutron magic number is evidently seen. Beyond $N = 34$, S_{2n} becomes negative and we therefore reach the drip-line at $N = 34$ for $Z = 14$. An extensive study of isotones also confirms the proton shell closure at $Z = 14$. Indeed, from the neutron single-particle structure seen in Fig. 1c, we find that the single-particle energy gaps found for $Z = 14$ are also maintained for the neutron number $N = 14$. Further, it is expected from the isospin symmetry considerations [12] that the mirror nuclei with $N = 14$ and $Z = 8$, 20, 28, 34 should also exhibit similar shell closures. Calculation results show that among these, the bound mirror nuclei ^{22}O and ^{34}Ca are indeed doubly magic, whereas the remaining ^{42}Ni and ^{48}Se are unbound due to an excessively large Coulomb repulsion of protons in these neutron-deficient nuclei.

We next note that, as can be seen from Fig. 1b depicting the separation energy, the S_{2n} value for the isotopes with $N = 30$–34 is rather small. The last neutrons in these nuclei fill the single-particle states $2p_{3/2}$ and $2p_{1/2}$, which lie close to the Fermi level near the continuum threshold. Just above these two states lies the $3s_{1/2}$ state, which remains in the continuum and does not come down to be bound even if more neutrons are added beyond $N = 34$. This is because it has no centrifugal barrier and its wave function is widely spread beyond the range of the potential. This fact consequently plays a crucial role in determining the neutron drip-line at $N = 34$, and we hence have ^{48}Si as the heaviest bound isotope for the element Si.

However, for the ^{44,46,48}Si isotopes, the wave functions of the last neutrons, which occupy the low-angular-momentum single-particle states $2p_{3/2}$ and $2p_{1/2}$ with a small centrifugal barrier, also have a considerable spread outside the potential region, albeit not to the extent the neutron $3s_{1/2}$ state mentioned above. Therefore, these neutrons are somewhat loosely bound. Consequently, a sudden increase in the neutron rms radius occurs for these isotopes, as is shown explicitly in Fig. 4 below. Also, because the last filled states for the ^{44,46,48}Si isotopes lie near the continuum threshold, these nuclei have small S_{2n} values. Moreover, since the single-particle states $2p_{3/2}$ and $2p_{1/2}$ have moderate single-particle energy gaps with respect to both the $1f_{7/2}$ and $3s_{1/2}$ single-particle states, we have the neutron number $N = 34$ as a magic number. A detailed study of the pairing interaction energy and the wave function of the single-particle states shows that the neutron single-particle state $2f_{5/2}$, which lies in the continuum at around 1.9 MeV, is a resonant state.

However, because it lies at a higher energy than the last filled states near the Fermi level, its contribution to the pairing correlation energy is rather negligible. Nevertheless, it is worthwhile at this point to emphasize the role of the location of such a resonant $2f_{5/2}$ state and that of the single-particle state $3s_{1/2}$: in fact, had this resonant state been at lower energy, its coupling to the nearby bound single-particle states (for example, $2p_{1/2}$ and $2p_{3/2}$) due to pairing interaction would be large. This would result in a further addition of neutrons to the resonant state and thus an extension in the position of the neutron drip-line beyond $N = 34$. Moreover, due to this role of accommodating more neutrons to keep the system bound, the resulting potential becomes conducive to bringing down the $3s_{1/2}$ state very close to the Fermi level and the coupling to the bound states to become partially or fully occupied. The filling of such an s state lying at the threshold of the contin-

uum gives rise to a halo formation in nuclei. Such a role of an single-particle resonant state combined with that of the position of an s state has been shown previously [26] to give rise to a large halo formation in the extremely neutron-rich Ca isotopes.

The results described above are further supported by the calculated proton and neutron density distributions, wherein it is seen that the densities fall off rapidly for the closed shell ^{22,28,34,42,48}Si isotopes compared with other isotopes with neutron density tails extending beyond the potential region. Also, the calculated radii are found to be in agreement with the available measurements [36–38]. Hence, the important prediction of these calculations is that in addition to the isotopes ^{28,34,42}Si being doubly magic, the ^{22}Si and ^{48}Si isotopes are also doubly magic. The isotope ^{48}Si lies on the neutron drip-line, whereas ^{22}Si falls on the proton drip-line. These two isotopes respectively constitute examples of neutron- and proton-rich doubly magic drip-line nuclei. So far, the heaviest isotope of Si observed experimentally is ^{43}Si, and it would be interesting to find an experimental confirmation of heavier isotopes, especially the doubly magic ^{48}Si at the neutron drip-line.

To check the possible dependence and sensitivity of the results on the force parameterization, we have also carried out these calculations using other popular RMF parameterizations, the NL3 and NLSH, given in detail in Refs. [21] and [22]. A comparison of the results for the Si isotopes shows that these forces (the TMA, NL3, and NLSH parameterizations) essentially yield similar results. Indeed, the results for the separation energy, proton and neutron radii, density profiles and drip lines, and so on are almost identical for all the Si isotopes. The same is found to be true for the proton and neutron single-particle spectra except for a small deviation in the NL3 results for the proton single-particle spectrum of ^{22}Si and that for the neutron single-particle spectrum of ^{42}Si compared with the TMA and NLSH results. To elaborate, whereas the TMA and NLSH results show shell closures for both protons and neutrons in ^{22}Si and ^{42}Si, the NL3 results indicate that ^{22}Si has shell closure only for neutrons, and similarly ^{42}Si exhibits shell closure only for protons. However, it follows from the detailed study of the pairing energy, single-particle pairing gaps, and occupancies of the single-particle levels that the deviation from the shell closures in these two nuclei for the NL3 force is in fact rather small.

Our findings of unusual magic numbers $N = 34$ at the neutron drip-line and $Z = 14$ at the proton drip-line are in agreement with the systematic RMF calculations
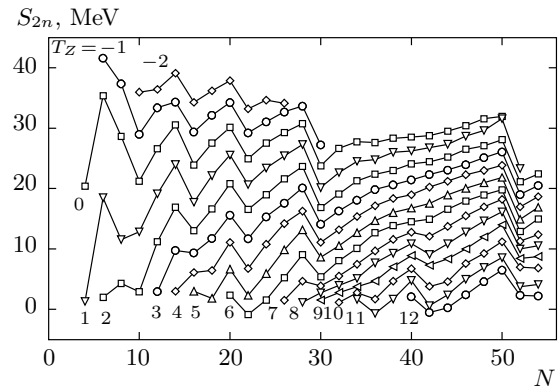

Fig. 2. Calculated results obtained in the RMF+BCS approach showing the variation of two-neutron separation energy S_{2n} with an increasing neutron number N. The lines connect the nuclei with the same isospin value $T_Z = (N - Z)/2 = -2, -1, 0, 1, 2, \ldots, 10, 11, 12$. At the magic numbers, a sudden decrease in the separation energy is evidently seen

including deformation in Ref. [30], whose results are tabulated in Table, which shows that the ^{22,48}Si nuclei have the spherical shape. Experimental measurement for the ^{22,48}Si isotope would be extremely interesting in order to test the drip-line and these new unusual shell closures.

The above encouraging description of the entire chain of Si isotopes in the spherical framework gave us strong motivation to extend these investigations to the entire chart of the nuclei up to the drip-lines, especially, to study the occurrence of shell closures, the existence of weakly bound nuclei, and the possibility of halo formation in detail. As has been demonstrated above, these features of nuclei are primarily governed by the single-particle structures, the location of possible resonant states, the coupling due to the pairing interaction between bound and unbound states, especially the resonant states near the Fermi level, and changes in the total number of protons and neutrons, which in turn govern the shape of proton and neutron potentials. Again, as in the case of Si isotopes, these studies have also been carried out in terms of pairing energy, two-neutron and two-proton separation energies (S_{2n} and S_{2p}), single-particle proton and neutron spectra, and rms radii and density distribution profiles for the protons and neutrons to obtain the magic numbers and to identify the halo formations.

As an illustration, Fig. 2 shows the two-neutron separation energy S_{2n} with an increasing neutron number N. The various curves in the figure connect the nuclei

Table. Doubly magic nuclei with their quadrupole deformation parameter for matter distribution β_{2m} [30]

Doubly magic nucleus	β_{2m}	Doubly magic nucleus	β_{2m}	Doubly magic nucleus	β_{2m}	Doubly magic nucleus	β_{2m}
$^{4}_{2}\text{He}_{2}$	0.00	$^{22}_{8}\text{O}_{14}$	0.00	$^{48}_{14}\text{Si}_{34}$	0.00	$^{78}_{28}\text{Ni}_{50}$	0.00
$^{8}_{2}\text{He}_{6}$	0.00	$^{24}_{8}\text{O}_{16}$	0.00	$^{34}_{20}\text{Ca}_{14}$	0.00	$^{98}_{28}\text{Ni}_{70}$	0.00
$^{12}_{6}\text{C}_{6}$	0.00	$^{28}_{8}\text{O}_{20}$	0.00	$^{40}_{20}\text{Ca}_{20}$	0.00	$^{116}_{34}\text{Se}_{84}$	0.00
$^{14}_{6}\text{C}_{8}$	0.00	$^{22}_{14}\text{Si}_{8}$	0.00	$^{48}_{20}\text{Ca}_{28}$	0.00	$^{100}_{50}\text{Sn}_{50}$	0.00
$^{22}_{6}\text{C}_{16}$	0.00	$^{28}_{14}\text{Si}_{14}$	0.34	$^{60}_{20}\text{Ca}_{40}$	0.00	$^{132}_{50}\text{Sn}_{82}$	0.00
$^{14}_{8}\text{O}_{6}$	0.00	$^{34}_{14}\text{Si}_{20}$	0.00	$^{48}_{28}\text{Ni}_{20}$	0.00	$^{176}_{50}\text{Sn}_{126}$	0.00
$^{16}_{8}\text{O}_{8}$	0.00	$^{42}_{14}\text{Si}_{28}$	0.37	$^{56}_{28}\text{Ni}_{28}$	0.00	$^{208}_{82}\text{Pb}_{126}$	0.00

with the same isospin component $T_Z = (N - Z)/2$ ranging from -2 to 12. In this figure, the results for nuclei with neutron numbers N only up to 54 are displayed. Plots of S_{2n} covering nuclei with higher N, and analogous plots for the two-proton separation energy S_{2p} with increasing Z values exhibit similar characteristics and are not displayed here in order to save space. In Fig. 2 and in similar plots for heavier nuclei, a sudden decrease in the two-neutron separation energies S_{2n} is clearly seen at the major shell closures corresponding to the traditional neutron magic numbers $N = 8, 20, 28, 50, 82, 126$. Analogously, a decrease is observed in the two-proton separation energies S_{2p} (not shown here) at the traditional proton magic numbers $Z = 8, 20, 28, 50, 82$. These major neutron and proton shells are generally seen to persist well into regions belonging to proton-rich and neutron-rich nuclei while approaching the drip-lines. For these magic numbers, the chains of bound isotopes and isotones are relatively large. Such magic numbers may be termed strong magic numbers. However, there are instances, especially in the neutron-rich cases, where a major shell structure is weakened and the associated magic number disappears with the emergence of a new magic number. For example, the present approach yields that for the neutron-rich Ca isotopes, the magicity for $N = 50$ disappears, while $N = 40$ becomes a new magic number. This is due to an appreciable gap between the $1f_{5/2}$ and $1g_{9/2}$ states as the $1g_{9/2}$ state is shifted upward closer to the $3s$–$2d$ shells. Indeed, as seen in Fig. 2, the neutron number $N = 40$ shows magicity for other nuclei corresponding to curves for T_Z values ranging from 7 to 12. Thus, $N = 40$ is found to be a magic number for the nuclei ^{56}S, ^{58}Ar, ^{60}Ca, ^{62}Ti, ^{64}Cr, and ^{66}Fe with Z values between 16 and 26.

In a similar manner, we find that nuclei in different regions of the periodic table lying between the beta stability line and the drip-lines exhibit shell closures at other N or/and Z values due to the variations in the neutron and proton single-particle structures with changing N or/and Z values.

Indeed, besides the traditional magic numbers, the lightest nuclei show magicity at $Z = 6$ for the neutron number from $N = 4$ to $N = 16$, and analogously at $N = 6$ for the proton number from $Z = 2$ to $Z = 8$ is found in our calculations. It appears that the magicity at $Z = 6$ and $N = 6$, and similarly for several other Z and N values up to 34, holds in a symmetric manner for the neutron-rich and proton-rich nuclei, although due to the Coulomb repulsion, highly proton-rich nuclei are found to be unbound in comparison to neutron-rich cases. The single-particle structure shows that in lighter nuclei, the occurrence of these magic numbers is caused by the increased spacing between the $1p_{3/2}$ and $1p_{1/2}$ states. Among these, the nuclei ^{8}He, ^{12}C and ^{14}O etc., appear to be doubly magic. Moving up, we find $Z = 14$ to be a magic number for all the isotopes with even N values ranging between 8 and 34. Among these, the $^{22,28,34,42,48}\text{Si}$ isotopes are predicted to be doubly magic, as is described in detail in the context of Si isotopes above. Similarly, $N = 14$ is found to be a magic number for nuclei with even Z values between 8 and 20, as can be seen in Fig. 2.

Moreover, taking $N = 14$ with $Z = 8, 14, 20$ provides doubly magic nuclei ^{22}O, ^{28}Si, and ^{34}Ca. Next, we find that $Z = 16$ is a proton magic number for the proton-rich isotopes $^{26-28}\text{S}$. Similarly, our calculations predict the appearance of $N = 16$ as a magic number for the neutron rich nuclei ^{22}C, ^{24}O, and ^{26}Ne, as is also seen in Fig. 2. Moreover, out of these three, ^{22}C and ^{24}O are observed to be doubly magic nuclei, which is in agreement with recent experiments [3–5]. The magicity at N or $Z = 16$ results due to the increased spacing of the single-particle energy levels $2s_{1/2}$

and $1d_{5/2}$ from the single-particle state $1d_{3/2}$. Further up, calculations show the magicity at $Z = 34$ for the neutron-rich isotopes ^{114,116}Se. Out of these two, the ^{116}Se isotope is found to be doubly magic. Similarly, $N = 34$ is found to be a magic number for neutron-rich nuclei with Z ranging from 12 to 16 due to the large spacing of neutron $2p_{3/2}$ and $2p_{1/2}$ states from the $1f_{5/2}$ state. With $Z = 14$, this yields the doubly magic nucleus ^{48}Si. Thus, interesting results of the calculations are the prediction of unusual proton magic numbers at $Z = 6, 14, 16, 34$, and neutron magic numbers at $N = 6, 14, 16, 34, 40, 70, 112$ in addition to the traditional magic numbers. In contrast to the neutron case, no proton magic numbers are predicted at $Z = 40, 70, 112$.

These predictions of doubly magic nuclei are also found to be consistent with the results in Ref. [30], showing no deformation for these nuclei, as can be seen in Table, where we tabulated the quadrupole deformation parameter for matter distribution β_{2m} for all predicted doubly magic nuclei by our RMF+BCS approach. The quadrupole deformation parameter has been calculated by assuming deformed nuclei of axially symmetric shapes [30]. Interestingly, except the ^{28,42}Si nuclei, all predicted doubly magic nuclei are of spherical shape, was the reason to analyze and discuss the results for these nuclei with negligible deformation in the framework of the spherical RMF+BCS description for convenience. In such a spherical framework, the contributions of neutron and proton single-particle states to the density profiles, pairing gaps, total pairing energy, etc., which are also equally important in the study of exotic phenomena, can be demonstrated with clarity.

The density profiles of the investigated nuclei show that the well-bound nuclei, which do not include nuclei close to drip-lines, exhibit rapid decrease in the radial neutron density ρ_n and proton density ρ_p distributions as the radial distance increases beyond the range of the nuclear potential. By contrast, the loosely bound neutron-rich nuclei due to spread in the single-particle wave functions of the loosely bound neutrons exhibit extended tails in their radial density distributions ρ_n, giving rise to a large skin thickness and even to a halo formation in some cases.

A similar situation in principle should occur also for the proton-rich loosely bound systems. But this is generally not the case because excessively proton-rich nuclei do not remain bound due to the Coulomb repulsion. In Fig. 3, to demonstrate that the density has a large spatial extension for loosely bound and especially for halo nuclei, we display the radial distances $r(\rho_n)$
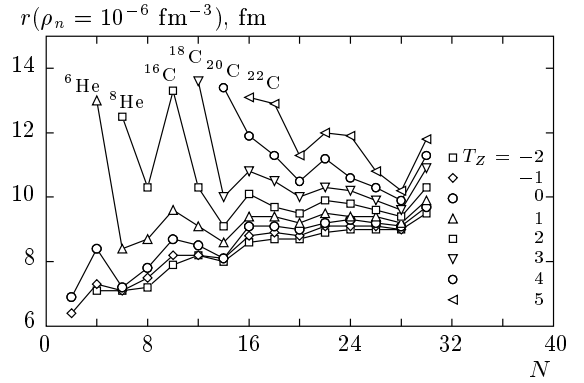

Fig. 3. Variation in the radial distances $r(\rho_n)$ for different nuclei at which the neutron density distribution ρ_n as a function of the increasing neutron number N diminishes to an arbitrarily chosen small value 10^{-6} fm^{-3}. The lines connecting different nuclei with the isospin value $T_Z = (N - Z)/2$ ranging from -2 to 5 are been drawn to guide the eyes

at which the neutron density value decreases to an arbitrarily chosen small value, for example, 10^{-6} fm^{-3}. This figure shows the results only for nuclei with the isospin component T_Z ranging from -2 to 5.

In Fig. 4, for some selected nuclei, we also display the radii for the proton and neutron distributions, r_p and r_n (along with the available experimental data), in order to show that for neutron-rich weakly bound systems and halo nuclei, there is a sudden jump in the growth of neutron radii in passing from one isotope to another. Indeed, it is found that the neutron density ρ_n for the lightest neutron-rich nuclei $^{6-10}$He, ^{14}Be, and $^{16-22}$C, etc., diminishes to the value 10^{-6} fm^{-3} only at a much larger radial distance $r(\rho_n) > 12$ fm, indicating its wide spatial extension with a slow fall off, as can be seen for some of these nuclei in Fig. 3. In what follows, we only briefly discuss the results of our calculations for the neutron-rich He, Be, and C isotopes for the purpose of illustration.

It can be seen from Fig. 3 that the radial distance $r(\rho_n)$ of about 7 fm for the neutron density fall off for ^{4}He suddenly jumps to about 13 fm for ^{6}He. This indicates a $2n$-halo formation with ^{4}He as the core. The calculated binding energies of ^{4}He and ^{6}He show only a minor gain of 1.31 MeV from ^{4}He to ^{6}He, in agreement with the experimental data for binding energy [35]. Because of the weakly bound structure, there is a sudden jump in the neutron distribution radius r_n from ^{4}He to ^{6}He, as can be seen in Fig. 4. The halo nature of the ^{6}He isotope is further supported by the following features. The neutron single-particle energy spectrum
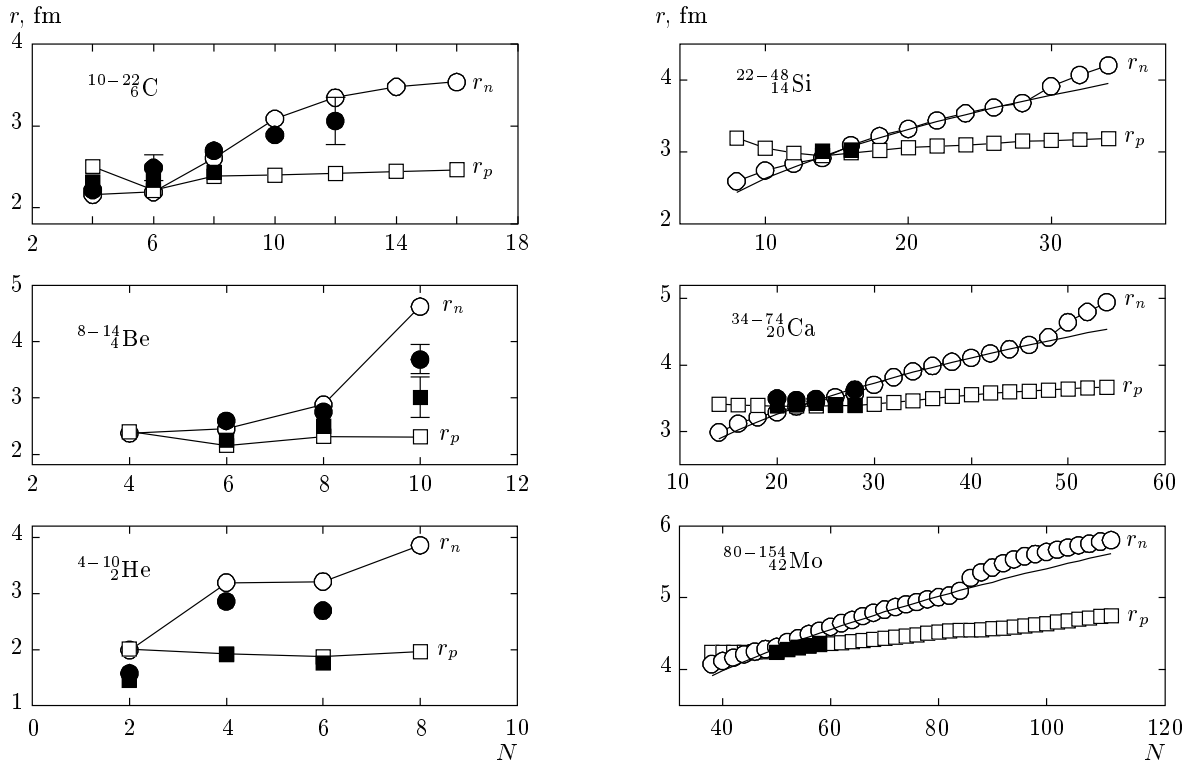
Fig. 4. Variation in the rms radii of neutron r_n and proton r_p distributions obtained in our RMF+BCS calculations for He, Be, C, Si, Ca, and Mo isotopes as a function of the increasing neutron number N. A sudden large increase in the neutron radii is observed for some isotopes. Available experimental data [6, 7, 36–40, 43] for the rms radii r_n and r_p are respectively shown with filled circles and squares for the purpose of comparison. In the plots for Si, Ca, and Mo isotopes, the solid line depicts a rough estimate for the neutron radius given by $r_n = r_0 N^{1/3}$, where the radius constant r_0 is chosen to provide the best fit to the theoretical results

shows that the single-particle state $1p_{3/2}$ occupied by the last two neutrons is located close to the zero energy, whereas the Fermi level also lies just below the continuum threshold.

Further addition of two neutrons to ^{6}He does not result in extra growth of the spatial extension of the neutron distribution. Consequently, for ^{8}He, the radial distance of the neutron density fall off $r(\rho_n)$ remains almost similar to that for ^{6}He, as is seen in Fig. 3. The calculated radii r_n for the neutron distributions for ^{6}He and ^{8}He are respectively 3.19 fm and 3.21 fm. This suggests that ^{8}He is not formed of ^{6}He as a core and two valence neutrons. In a recent measurement using the ^{7}Li$(p, 2p)^6$He reaction, the r_n value 2.85 fm was deduced for ^{6}He in [39]. Previous measurements [6] yielded $r_n = 2.61$ fm for ^{6}He and $r_n = 2.64$ fm for ^{8}He. Our calculated r_n values compare with these measurements reasonably well, as is shown in Fig. 4. Also, it is found that for the isotope ^{8}He, the neutron number $N = 6$ is a magic number. This makes ^{8}He a doubly magic system. Our detailed results indeed show

that addition of two neutrons to ^{6}He tends to provide just a little more binding and stability for the ^{8}He nucleus without increasing its spatial dimension. This is also reflected in the rms charge radii of the isotopes ^{6}He and ^{8}He. The calculated rms charge radius of ^{8}He is found to be $r_{ch} = 1.98$ fm, to be compared with $r_{ch} = 2.05$ fm for ^{6}He. It is interesting to note that our calculated values of rms charge radii compare very well with the recently measured values $r_{ch} = 1.93$ fm for ^{8}He and $r_{ch} = 2.07$ fm for ^{6}He [40]. A slight decrease in the rms charge radius from ^{6}He to ^{8}He is indicative of a difference in the correlations of the $2n + ^4$He system compared to the $2n + 2n + ^4$He system. An interpretation of ^{8}He as a weakly bound halo-like system [40, 41] of $(2n + 2n)$ plus ^{4}He as a core appears to be consistent with our calculations. Thus, ^{8}He appears to be an interesting system in the sense that it is a weakly bound doubly magic super-neutron-rich isotope of He with halo characteristics located at the neutron drip-line.

If two more neutrons are added to ^{8}He, it is found

that the resulting isotope ^{10}He becomes just unbound via the two-neutron emission. This is because the neutron single-particle state $1p_{1/2}$, which lies in the continuum just above the zero energy for all $^{4-8}$He isotopes, remains almost unaffected by increasing the number of neutrons. It moves down only to become weakly bound with an single-particle energy of 0.57 MeV while the neutron Fermi level moves up and now lies in the continuum at $\epsilon_F = 0.14$ MeV. The next single-particle state above $1p_{1/2}$ is the $2s_{1/2}$ state lying close to the continuum threshold at 0.17 MeV. The total binding energy of ^{10}He is found to be 29.68 MeV, to be compared with the binding energy of 30.75 MeV for ^{8}He. Therefore, ^{10}He is unstable with respect to $2n$-emission by $S_{2n} = 1.08$ MeV.

Our results are consistent with the experiments [35, 42] on spectroscopy of ^{10}He. The isotope ^{10}He is found to have an excessively large extension of the neutron density distribution, resulting in the large value of radial distance $r(\rho_n) = 16$ fm for density fall off, and is not shown in Fig. 3 because it lies outside the scale of the plot. Again, a sudden jump in the neutron radius r_n is also obtained in passing from ^{8}He to ^{10}He, as can be seen in Fig. 4. Moreover, the neutron single-particle spectrum shows that for ^{10}He, the neutron number $N = 8$ remains a magic number. Consequently, ^{10}He is also a doubly magic isotope like ^{8}He. These features characterize a spatially extended configuration for ^{10}He unbound via $2n$-emission.

Calculations for the Be isotopes $^{6-14}$Be and C isotopes $^{8-22}$C yield results with features similar to those of the He isotopes. The isotope ^{6}Be is found to be unbound via the emission of two protons in agreement with the measurements in [35]. With the addition of two neutrons, in passing from ^{6}Be to ^{8}Be, the proton mean-field potential becomes deep enough to provide stability to ^{8}Be. The results for the isotope ^{10}Be show the neutron number $N = 6$ to be a magic number. In the case of ^{12}Be, an appreciable gap of 4.3 MeV between the single-particle state $1p_{1/2}$ and the next higher single-particle state $2s_{1/2}$ helps retain the usual magicity for the neutron number $N = 8$.

The next isotope ^{14}Be is found to exhibit an extended neutron density distribution. The value for the density fall-off radius $r(\rho_n)$ is quite large, and is not shown explicitly in Fig. 3 because it lies outside the scale of the plot. The radius for the neutron distribution r_n shows a sudden jump from ^{12}Be to ^{14}Be, as can be seen in Fig. 4. These features characterize the $2n$-halo formation in ^{14}Be. The last two neutrons are found to occupy the single-particle state $2s_{1/2}$. This neutron single-particle state lies just below the con-

tinuum threshold at -0.29 MeV, whereas the neutron Fermi energy is found to be -0.06 MeV. The occupancy of the loosely bound single-particle state $2s_{1/2}$ and the location of the Fermi level very close to the continuum together provide extremely favorable conditions for the halo formation in ^{14}Be. However, the calculated rms neutron distribution radius r_n is somewhat larger than that extracted from the interaction cross section measurements [6, 7, 43], as can be seen in Fig. 4. A larger value of the calculated rms neutron radius in comparison with the experimental data indicates that the isotope ^{14}Be is slightly underbound. Indeed, the calculated binding energy value is found to be smaller by about 1.8 MeV than the experimental value 69.98 MeV.

Our calculations for the isotopes $^{8-22}$C show that the proton number $Z = 6$ remains a magic number for the entire chain of isotopes due to a large energy gap between the proton single-particle states $1p_{3/2}$ and $1p_{1/2}$. Similarly, the neutron numbers $N = 6$ and $N = 16$ are also found to be magic numbers in addition to the traditional magic numbers 2 and 8. Moreover, calculations show that the isotope ^{8}C is unbound to 2-proton emission, and the isotope ^{22}C lies at the two-neutron drip-line. These findings along with the calculated two-neutron separation energy for the C isotopes are found to be in agreement with the available measurements [35].

A comparison of the shell gaps for the isotopes ^{12}C and ^{14}C suggests that the neutron number $N = 6$ provides a much stronger magicity than the magicity for $N = 8$, a feature also found to be true for the He and Be isotopes. Consequently, the isotope ^{12}C has the largest binding energy per nucleon, and a relatively negligible growth in the neutron distribution radius from ^{10}C to ^{12}C in comparison to that from ^{12}C to ^{14}C, as can be seen in Fig. 4. A comparison of the calculated rms proton and neutron radii with the available experimental data depicted in Fig. 4 shows a reasonably good agreement with measurements [7, 37, 43]. However, data on the neutron radius r_n for the isotopes ^{12,18}C have large error bars. It is gratifying to note that for the isotopes $^{10-22}$C, the relativistic Hartree–Bogoliubov (RHB) approach, which provides a unified description of mean-field and pairing correlations, yields results [44] that are very close to those obtained in the present RMF+BCS calculations.

A detailed analysis of the calculated results for the $^{10-22}$C isotopes shows that the neutron-rich $^{16-22}$C isotopes are examples of a somewhat loosely bound system due to simultaneous and gradual filling in of the neutron single-particle $2s_{1/2}$ and resonant $1d_{5/2}$ states
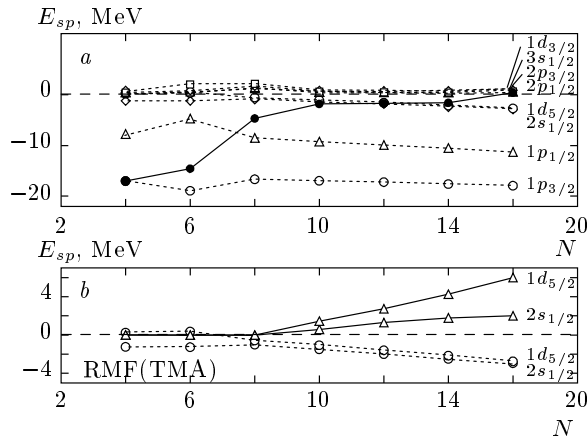
Fig. 5. *a*) Variation of the neutron single-particle energies obtained with the TMA force for the carbon isotopes $^{10-22}$C as the neutron number increases. The neutron Fermi energy is shown by filled circles connected by solid line to guide the eye. *b*) Variation of the position (○) and occupancy (△) (the number of neutrons occupying the levels) of the neutron $1d_{5/2}$ and $2s_{1/2}$ single-particle states in the $^{10-22}$C isotopes as the neutron number increases

in these isotopes. In Fig. 5*a*, to elucidate this point, we display the variation in the neutron single-particle spectrum as the neutron number N increases. The figure also shows the position of the Fermi level. Figure 5*b* explicitly shows the variation in the position of neutron $2s_{1/2}$ and $1d_{5/2}$ single-particle states along with their occupancy in terms of the number of neutrons. It is found that the neutron $1d_{5/2}$ single-particle state, which lies just above the continuum threshold in $^{10-12}$C, is a resonant state having a large pairing gap $\Delta(1d_{5/2})$. As the number of neutrons increases, it moves down and becomes bound, as can be seen in Fig. 5*b*.

Characteristically, the wave function of the resonant $1d_{5/2}$ state is always confined within the potential region and therefore has an appreciable overlap with the other lower bound states. This results in an increased pairing gap and an enhanced contribution to the pairing energy. Therefore, the neutron $1d_{5/2}$ state, which always lies above the $2s_{1/2}$ state, begins to be partially occupied already in ^{16}C, even before the $2s_{1/2}$ state is totally filled. This simultaneous filling of the two states continues until the drip-line isotope ^{22}C is reached when both the $2s_{1/2}$ and $1d_{5/2}$ are totally occupied. The simultaneous filling of single-particle states helps in accommodating more neutrons with a comparatively small increase in the total binding energy; con-

sequently, we have somewhat loosely bound neutron-rich isotopes $^{16-22}$C.

The neutron $2s_{1/2}$ state, which begins to be occupied in the isotope ^{16}C, essentially gives rise to an extended neutron density distribution. Consequently, a large value of the density fall-off radius $r(\rho_n)$ is obtained for ^{16}C in comparison to that for ^{14}C, as is evidently seen from Fig. 3. Correspondingly, an enhancement in the rms radius r_n for the neutron distribution is also found in passing from ^{14}C to ^{16}C, as is evident from Fig. 4. The matter density of ^{16}C extracted from cross section measurements [6, 45, 46] also supports an extended neutron tail in the isotope ^{16}C. As can be seen from Fig. 5, the $2s_{1/2}$ state tends to become more bound with the increasing number of neutrons beyond ^{16}C, and hence it becomes unlikely to have halo formation in the heavier neutron-rich $^{18-22}$C isotopes. With a further addition of neutrons to ^{16}C, the density fall-off radius $r(\rho_n)$ remains almost unchanged for the isotopes $^{18-22}$C, as can be seen in Fig. 3. For the drip-line nucleus ^{22}C, the Fermi level moves just above the continuum threshold at $\epsilon_F = 0.43$ MeV, as can be seen in Fig. 5*a*. The neutron single-particle spectrum of the ^{22}C isotope shows that the single-particle state next to the fully occupied $1d_{5/2}$ state is higher in energy by about 3.2 MeV in the continuum. Due to such a large gap in the single-particle energy, the neutron number $N = 16$ shows magicity. Thus, ^{22}C represents another example of a spherical drip-line nucleus for which the neutrons are somewhat loosely bound. It is gratifying to note that this result for ^{22}C is in agreement with the recent experiment in [5].

It is evident from the above discussion that the ground-state properties of the even–even $^{16-22}$C isotopes are to an extent influenced by the gradual and simultaneous filling of the close-lying neutron $2s_{1/2}$ and $1d_{5/2}$ single-particle states. These isotopes are somewhat weakly bound due to the wide spatial spread in the wave function of the $2s_{1/2}$ state. The single-particle spectrum in Fig. 5 also suggests that the odd-neutron isotopes $^{15-21}$C with neutron numbers $N = 9$, 11, 13, 15 should be even more weakly bound than even-neutron (nonmagic) isotopes because the binding energy of even-neutron isotopes has a sizable additional contribution from the pairing energy of the last two neutrons besides the single-particle energy contributions. This is especially interesting for the isotope ^{15}C since the neutron single-particle spectrum in Fig. 5 evidently provides support to a halo-like formation for this isotope because the odd neutron fills the $2s_{1/2}$ state while it lies close to the zero energy as well as the Fermi level.

To check the force parameter dependence of these results for He, Be, and C isotopes, we repeated these RMF+BCS calculations using the NL3 and NLSH parameters [21, 22]. The calculated results, apart from minor details, remained essentially close to those obtained using the TMA force parameters. However, calculations in [47, 48], similar to those in Ref. [30] including the deformation degree of freedom, show that some of the Be and C isotopes are highly deformed. Nevertheless, our main conclusions remain unchanged.

For oxygen isotopes, the calculations show that ^{14,16,22,24}O are doubly magic nuclei. The isotopes ^{26,28}O are found to be bound, which is at variance with the experimental data [35], though consistent with the results of other mean-field calculations including those carried out with the deformation degree of freedom [30]. This discrepancy with respect to measurements needs separate investigations.

The weakly bound structures and halos in the neutron-rich isotopes of He, Be, and C demonstrated in Fig. 4 are the lightest in the chains of nuclei with the isospin component value T_Z lying between 1 and 5 (see Fig. 3). Besides these, the neutron-rich isotopes $^{44-48}$Si described earlier provide a similar example of the occurrence of loosely bound systems with large neutron skin, as is shown in Fig. 4. The possibility of halo formation is found to be lower in heavier nuclei. However, for several neutron-rich nuclei, for example, the heavier isotopes of Ca, Zr, Mo, etc., in the vicinity of the neutron drip-line, it is found that further addition of neutrons causes a rapid increase in the neutron rms radius with a very small increase in the binding energy ($S_{2n} \approx 20$ keV to 1.5 MeV), thereby indicating the occurrence of very weakly bound structures, as is shown in Fig. 4 for the Ca and Mo nuclei.

In the case of neutron-rich Ca isotopes, this is essentially caused by the gradual filling of the loosely bound single-particle neutron state $3s_{1/2}$ and the resonant $1g_{9/2}$ state [26]. Similarly, weakly bound isotopes of neutron-rich Mo isotopes, as also in the case of Zr isotopes, are found to occur due to the gradual filling of the resonant $2f_{7/2}$, $2f_{5/2}$, and $1h_{9/2}$ states together with the loosely bound single-particle neutron states $3p_{1/2}$ and $3p_{3/2}$. The gradual occupancy commences at $N = 84$ in the isotope ^{126}Mo. As mentioned above, preference for the occupancy of resonant states stems from the fact that in contrast to loosely bound single-particle states, the resonant states have their wave functions entirely confined inside the potential well, similarly to a bound state. This interesting phenomenon of accommodating several additional neutrons with an almost negligible increase in bind-

ing energy is found to be due to pairing correlations [26]. Also, due to the widely extended single-particle wave function of the $3p_{1/2}$ and $3p_{3/2}$ states, a sudden increase in the neutron rms radius occurs for the isotope ^{126}Mo at $N = 84$, as can be seen in the plot for the Mo isotopes in Fig. 4. The gradual filling of these states is completed at $N = 112$, which corresponds to the drip-line isotope ^{154}Mo. However, in Mo isotopes, the single-particle state $4s_{1/2}$ remains in the continuum throughout without being occupied. This prohibits excessive growth in the rms neutron radius. The details of these results will be published elsewhere.

4. SUMMARY

Inspired by the recent experiments [1–5] indicating doubly magic nuclei and halo nuclei near the drip-line and encouraged by the success of our relativistic mean-field (RMF) plus state-dependent BCS approach to the description of the ground-state properties of drip-line nuclei [26, 28], we have further developed this approach, across the entire periodic table, to explore the unusual shell closures, doubly magic nuclei, loosely bound structures, and halo formation in exotic nuclei.

We used the Lagrangian density with nonlinear terms for the σ and ω mesons along with the TMA force parameters [18]. State-dependent BCS calculations with a delta-function interaction with the same interaction strength have been performed for the pairing correlation energy. The calculated results comprising the systematics for the pairing energy, pairing gaps, two-neutron and two-proton separation energies, neutron and proton radii, and the neutron and proton density distribution profiles have been analyzed to predict the possible magic numbers and to explore and examine the occurrence of weakly bound nuclei including the formation of halos.

In particular, the results for the entire chain of Si isotopes show that the proton number $Z = 14$ represents a shell closure throughout up to the neutron drip-line, which is found to be at $N = 34$. More interestingly, it has been found that the isotopes ^{22,28,34,42,48}Si are doubly magic, indicating persistence of the neutron shell closure at $N = 8$, 14, 20, 28, 34. These findings, especially the fact that the heaviest and highly neutron-rich ^{48}Si nucleus is doubly magic, need experimental confirmation.

Our calculations, especially in the case of neutron-rich nuclei, show that the interplay of (i) variation of energy of the proton and neutron single-particle states due to change in the number of protons and neutrons,

(ii) the position of resonant states, and (iii) the positions and angular momenta of the single-particle states lying near the continuum threshold greatly influences the shell closures and hence the magicity in nuclei. The filling of single-particle s- or p-states lying close to the continuum threshold gives rise to a sudden increase in the rms radius, leading to a loosely bound system or even a halo formation. Similarly, the low-lying resonant states, especially those with high angular momenta, help in accommodating an excessively large number of neutrons, extending the neutron drip line to extremely neutron-rich isotopes. Indeed, among the lightest nuclei, the isotopes $^{6-8}$He and ^{14}Be exhibit halo-like characteristics with wide spatial extensions in neutron densities. Also, the neutron-rich carbon isotopes $^{16-22}$C are found to represent a weakly bound system due to the interplay of the $2s_{1/2}$ and resonant $1d_{5/2}$ states lying close to the continuum threshold. The neutron-rich Si isotopes ^{44,46,48}Si provide another example of loosely bound isotopes near the drip-line due to the filling of the low-angular-momentum single-particles states $2p_{3/2}$ and $2p_{1/2}$. Several medium-heavy nuclei are found to exhibit loosely bound neutron-rich isotopes due to the interplay of the resonant and weakly bound single-particle states, as was described briefly in the case of Ca and Mo isotopes.

Our calculations predict the unusual proton magic numbers at $Z = 6$, 14, 16, 34 and unusual neutron magic numbers at $N = 6$, 14, 16, 34, 40, 70, 112. These results are found to be consistent with the experimental systematics [35] of two-proton S_{2p} and two-neutron S_{2n} separation energies.

REFERENCES

1. C. B. Hinke et al., Nature **486**, 341 (2012).

2. R. V. F. Janssens, Nature **459**, 1069 (2009).

3. R. Kanungo et al., Phys. Rev. Lett. **102**, 152501 (2009).

4. C. R. Hoffman et al., Phys. Lett. B **672**, 17 (2009).

5. K. Tanaka et al., Phys. Rev. Lett. **104**, 62701 (2010).

6. I. Tanihata, J. Phys. G **22**, 157 (1996); I. Tanihata et al., Comp. Ren. Phys. **437** (2003); Phys. Lett. B **512**, 261 (2001).

7. A. Ozawa, T. Kobayashi, T. Suzuki, K. Yoshida, and I. Tanihata, Phys. Rev. Lett. **84**, 5493 (2000); A. Ozawa et al., Nucl. Phys. A **709**, 60 (2002).

8. A. Jensen, K. Riisager, D. V. Fadarov, and E. Garrido, Rev. Mod. Phys. **76**, 215 (2004) and reference therein; A. S. Jensen and K. Riisager, Phys. Lett. B **480**, 39 (2000); P. G. Hansen and A. S. Jensen, Ann. Rev. Nucl. Part. Sci. **45**, 591 (1995).

9. A. B. Migdal, J. Nucl. Phys. **16**, 238 (1973).

10. S. Dasgupta, I. Mazumdar, and V. S. Bhasin, Phys. Rev. C **50**, 551(R) (1994).

11. G. Bertsch, H. Esbensen, and A. Sustich, Phys. Rev. C **42**, 758 (1990); G. Bertsch and J. Fooxwell, Phys. Rev. C **41**, 1300 (1990).

12. T. Otsuka et al., Phys. Rev. Lett. **87**, 082502 (2001).

13. J. Dobaczewski et al., Phys. Rev. C **53**, 2809 (1996); K. Bennaceur, J. Dobaczewski, and M. Ploszajczak, Phys. Lett. B **496**, 154 (2000).

14. M. Grasso et al., Phys. Rev. C **64**, 064321 (2001).

15. B. D. Serot and J. D. Walecka, Adv. Nucl. Phys. **16**, 1 (1986).

16. P. G. Reinhard, Rep. Progr. Phys. **52**, 439 (1989) and references therein.

17. P. G. Reinhard, M. Rufa, J. Marhun, W. Greiner, and J. Friedrich, Z. Phys. A **323**, 13 (1986); S. Mizutori, J. Dobaczewski, G. A. Lalazissis, W. Nazarewicz, and P. G. Reinhard, Phys. Rev. C **61**, 044326 (2000).

18. Y. Sugahara and H. Toki, Nucl. Phys. A **579**, 557 (1994); Y. Sugahara, Ph. D. Thesis, Tokyo Metropolitan University (1995).

19. R. Brockman and H. Toki, Phys. Rev. Lett. **68**, 3408 (1992).

20. P. Ring, Nucl. Part. Phys. **24**, 1467 (1998); D. Veretenar, N. Paar, T. Niksic, and P. Ring, Phys. Rev. Lett. **91**, 262502 (2003).

21. G. A. Lalazissis, D. Vretenar, and P. Ring, Phys. Rev. C **57**, 2294 (1998).

22. M. M. Sharma, M. A. Nagarajan, and P. Ring, Phys. Lett. B **312**, 377 (1993).

23. M. Del Estal, M. Contelles, X. Vinas, and S. K. Patra, Phys. Rev. C **63**, 044321 (2001).

24. J. Meng, Phys. Rev. C **57**, 1229 (1998); Nucl. Phys. A **635**, 3 (1998).

25. J. Meng, H. Toki, J. Y. Zeng, S. Q. Zhang, and S. G. Zhou, Phys. Rev. C **65**, 041302(R) (2002); J. Meng, H. Toki, S. G. Zhou, S. Q. Zhang, W. H. Lang, and L. S. Geng, Progr. Part. Nucl. Phys. C **57**, 470 (2006).

26. H. L. Yadav, M. Kaushik, and H. Toki, Int. J. Mod. Phys. E **13**, 647 (2004).

27. H. L. Yadav, S. Sugimoto, and H. Toki, Mod. Phys. Lett. A **17**, 2523 (2002).

28. M. Kaushik, D. Singh, and H. L. Yadav, Acta Phys. Slov. **5**, No. 2, 181 (2005).

29. B. G. Todd-Rutel, J. Piekarewicz, and P. D. Cottle, Phys. Rev. C **69**, 021301 (2004).

30. L. S. Geng, Ph. D. Thesis, RCNP, Osaka University, Osaka (2005); L. S. Geng, H. Toki, S. Sugimoto, and J. Meng, Progr. Theor. Phys. **110**, 921 (2003).

31. A. M Lane, *Nuclear Theory*, Benjamin (1964).

32. P. Ring and P. Schuck, *The Nuclear Many-Body Problem*, Springer, Berlin (1980).

33. G. F. Bertsch and H. Esbensen, Ann. Phys. **209**, 327 (1991).

34. A. B. Migdal, *Theory of Finite Fermi Systems and Applications to Atomic Nuclei*, Interscience, New York (1967).

35. G. Audi, A. H. Wapstra, and C. Thibault, Nucl. Phys. A **729**, 337 (2003).

36. G. Fricke et al., Phys. Rev. **45**, 80 (1992).

37. H. de Vries, C. W. de Jager, and C. de Vries, At. Data Nucl. Data Tables **36**, 495 (1987).

38. C. J. Batty, E. Friedman, H. J. Gils, and H. Rebel, Adv. Nucl. Phys. **19**, 1 (1989).

39. V. B. Shostak et al., Phys. Rev. C **63**, 017602 (2000).

40. P. Mueller et al., Phys. Rev. Lett. **99**, 252501 (2007).

41. O. A. Kiselev et al., Eur. Phys. J. A **25**, Suppl. 1, 215 (2005).

42. A. N. Ostrowski et al., Phys. Lett. B **338**, 13 (1994).

43. E. Liatard et al., Europhys. Lett. **13**, 401 (1990).

44. W. Pschl, D. Vretenar, G. A. Lalazissis, and P. Ring, Phys. Rev. Lett. **79**, 3841 (1997).

45. T. Zheng et al., Nucl. Phys. A **709**, 103 (2002).

46. T. Yamaguchi et al., Nucl. Phys. A **734**, E73 (2004).

47. M. M. Sharma, S. Mythili, and A. R. Farhan, Phys. Rev. C **59**, 1379 (1998).

48. Z. Ren, Z. Y. Zhu, Y. H. Cai, and Gongou Xu, Nucl. Phys. A **605**, 75 (1996).